nature communications

Article

https://doi.org/10.1038/s41467-025-57224-8

Electrically-driven reversible phonon transport manipulation in two-dimensional heterostructures

Received: 5 September 2024

Accepted: 15 February 2025

Published online: 25 February 2025

Check for updates

Yufei Sheng[1,6], Hongxin Zhu[2,6], Siqi Xie[2], Qian Lv[3], Huaqing Xie[4], Haidong Wang[2] ✉, Ruitao Lv[3,5] ✉ & Hua Bao[1] ✉

Phonon transport manipulation is crucial for various technological applications, such as thermal management in electronic devices, thermoelectric energy conversion, and thermal insulation. However, to date, viable approaches for manipulating phonon transport remain limited, particularly in achieving reversible manipulation. Here, we achieve reversible manipulation of phonon transport in a monolayer $MoSe_2$-WSe_2 heterojunction, by modulating phonon thermal conductivity through the switching of bias voltage. The measured thermal conductivity under electrical forward bias is significantly lower than that observed under reverse cutoff. This effect becomes more pronounced with decreasing temperature. Through theoretical modeling supported by device simulation and first-principles calculation, the decrease in thermal conductivity under forward bias can be elucidated by higher carrier concentrations and electron temperatures. Our results provide an electrically-driven phonon transport manipulation approach, potentially opening up possibilities for dynamical and reversible thermal design in advanced semiconductor technologies.

Phonon transport, governing the heat conduction in nonmetallic crystalline materials, has garnered widespread attention in various advanced technologies, including thermal management[1,2], energy conversion[3], and the design of materials for extreme environments[4]. Effectively manipulating phonon transport is highly desirable for enhancing the functionalities and performance of these applications, yet its realization poses significant challenges[5,6]. Strategies to manipulate phonon transport typically involve altering specific phonon scattering processes, consequently leading to changes in phonon thermal conductivity[6,7]. In crystalline materials, the primary scattering processes for phonons include phonon-boundary scattering, phonon-phonon scattering, phonon-impurity/defect scattering, and phonon interactions with electrons[8,9]. Extensive prior research has attempted to alter phonon-boundary/phonon/impurity/defect scattering by modifying lattice structures, introducing approaches such as nanostructure construction[10,11], pressure tuning[12], strain engineering[13], and impurity/defect engineering[14,15]. These approaches have achieved alterations in phonon thermal conductivity. However, due to changes in intrinsic material properties[6,16,17] and the typically irreversible nature of lattice structural modifications[18], active and reversible phonon transport manipulation proves exceptionally challenging.

A more promising approach for achieving reversible phonon transport manipulation is by adjusting the phonon-electron scattering

[1]Global Institute of Future Technology, Shanghai Jiao Tong University, Shanghai, China. [2]Department of Engineering Mechanics, Key Laboratory for Thermal Science and Power Engineering of Ministry of Education, Tsinghua University, Beijing, China. [3]State Key Laboratory of New Ceramics and Fine Processing, School of Materials Science and Engineering, Tsinghua University, Beijing, China. [4]School of Energy and Materials, Shanghai Polytechnic University, Shanghai, China. [5]Key Laboratory of Advanced Materials (Ministry of Education), School of Materials Science and Engineering, Tsinghua University, Beijing, China. [6]These authors contributed equally: Yufei Sheng, Hongxin Zhu. ✉e-mail: hdwang@tsinghua.edu.cn; lvruitao@tsinghua.edu.cn; hua.bao@sjtu.edu.cn

processes[19,20], as electrons exhibit a rapid response to the external field and the lattice structure remains nearly unchanged[21]. Prior theoretical studies have confirmed the significant impact of phonon-electron scattering on phonon thermal conductivity in semiconductor materials[22,23]. Especially in two-dimensional (2D) semiconductor materials which have broad prospective applications in electronic devices, optoelectronic devices, and energy conversion[24–27], the influence of electron-phonon scattering on phonon thermal conductivity can be comparable to that of phonon-phonon scattering even at room temperature[28] and moderate carrier concentrations[29,30]. However, to date, effective experimental approaches for utilizing the electrical response characteristics of electrons to manipulate phonon transport remain unexplored.

Here, we achieve active and reversible manipulation of phonon transport in a 2D semiconductor $MoSe_2$-WSe_2 heterojunction by modulating the electron-phonon scattering processes through tuning bias voltages. We construct the heterojunction with electrical rectification effects using atmospheric pressure chemical vapor deposition method. Phonon thermal conductivity values of the heterojunction under electrical forward bias and reverse cutoff are measured using the H-type sensor method. The results indicate that the thermal conductivity under forward bias is lower than that under reverse cutoff. This difference amplifies with decreasing temperature, reaching a 13.8% decrease in thermal conductivity under forward bias compared to reverse cutoff at an ambient temperature of 258 K. The thermal conductivity is actively and reversibly manipulated by changing the bias voltage magnitude and direction over the applied voltage range of −20 to +15 V in the experiment. By combining device simulation with an effective first-principles-based model, we find this manipulation can be theoretically explained as varying strengths of phonon-electron scattering under different bias voltages.

Results

Fabrication and thermal conductivity measurement of $MoSe_2$-WSe_2 lateral heterojunctions

As shown in Fig. 1a, b, the monolayer $MoSe_2$-WSe_2 lateral heterostructure samples were synthesized by atmospheric pressure chemical vapor deposition (AP-CVD) route as reported in our previous work[31,32], and a higher current density was achieved by interface doping. We deposited two gold sensors with a thickness of 100 nm on top of the samples by physical vapor deposition (PVD), and the sensors were designed in an H-shape to facilitate the measurement of their thermal conductivities[33]. As a comparison, the monolayer pure $MoSe_2$ and monolayer pure WSe_2 were synthesized via the chemical vapor deposition (CVD) technique[34,35], shown in Fig. 1c, d. Subsequently, a 370-nm-thick polymethyl methacrylate (PMMA) film was spin-coated on top of the samples for transfer to the suspended H-type gold electrodes. To avoid potential damage caused by the limited mechanical strength of transition metal dichalcogenide (TMD) materials, the PMMA layers atop the pure $MoSe_2$ and pure WSe_2 were preserved to serve as a supportive matrix, with their triangular profiles clearly shown in the SEM images (Fig. 1c, d). Similarly, a 300-nm-thick SiO_2 layer film was underneath the $MoSe_2$-WSe_2 heterostructure to provide necessary support. Moreover, the silicon substrate underlying all the samples was deeply etched to a depth exceeding 2.5 μm, ensuring the sensor remained suspended and avoiding heat leakage from the silicon substrate. This design feature enhanced the gold sensor's responsiveness to heat flow passing through the sample, thereby optimizing its sensitivity for thermal detection applications.

The measurement methodology is predicated on the utilization of two gold sensors, which serve as heaters while concurrently delivering precise temperature measurements (temperature resolution reaches 0.01 K). In this experimental setup, a large current passed through one gold sensor to heat the sample, while a comparatively weaker current

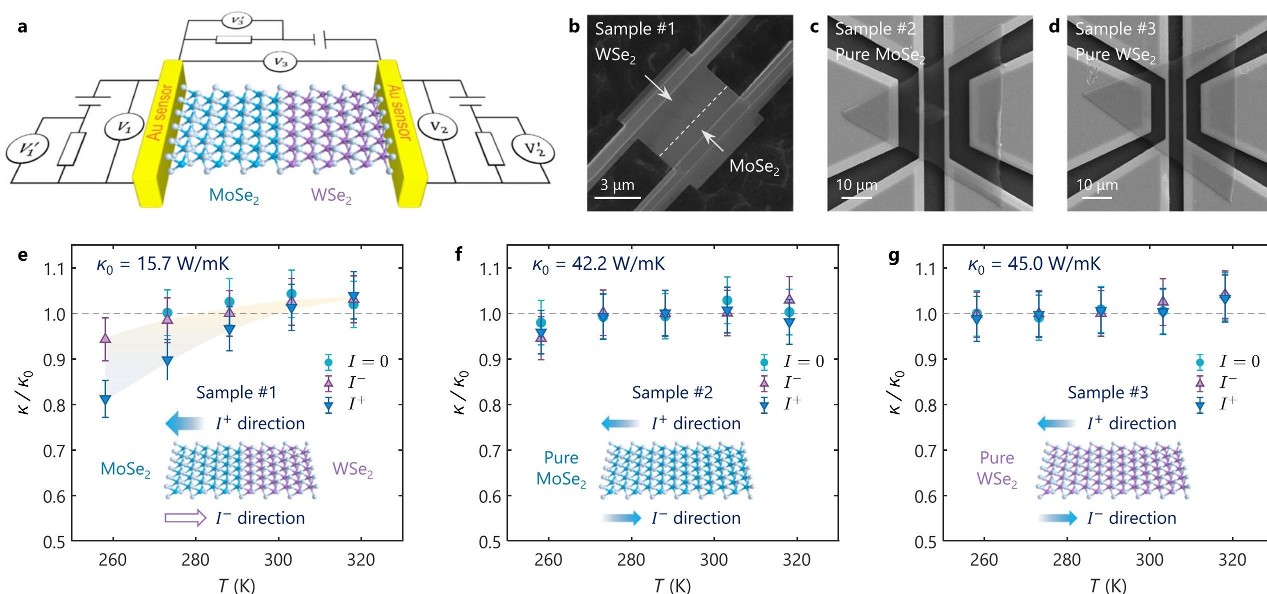

Fig. 1 | Experimental measurement circuit and thermal conductivity changes of $MoSe_2$-WSe_2 lateral heterojunctions under bias currents. a Schematic illustration for measuring the thermal conductivity. V_1, V_2, and V_3 are used to measure the voltage applied to the two gold sensors and the bias voltage across the sample respectively. V_1', V_2', and V_3' are used to measure the voltage of the three standard resistors respectively in order to obtain current in each circuit. By controlling the value of V_3, zero voltage bias, forward voltage bias and reverse voltage bias can be achieved. **b** Scanning electron microscope (SEM) image of the monolayer $MoSe_2$-WSe_2 lateral heterostructure sample (Sample #1). SEM images of monolayer pure $MoSe_2$ (Sample #2) (**c**) and monolayer pure WSe_2 (Sample #3) (**d**), respectively. The measured thermal conductivities of $MoSe_2$-WSe_2 lateral heterojunction (**e**), pure $MoSe_2$ (**f**), and pure WSe_2 (**g**) at different bias voltages, within a temperature range of 258–318 K, respectively. In each figure, the circle, upper triangle, and lower triangle patterns represent zero bias voltage, reverse bias voltage, and forward bias voltage respectively. κ_0 corresponds to the thermal conductivity under reverse bias at 288 K. Error bars show experimental uncertainties of ±5%. The shaded region in (**e**) highlights the difference in thermal conductivity under forward and reverse bias conditions. Part (**b**) reprinted with the permission from ref. 31, AAAS.

was applied to the other sensor to monitor the attendant temperature increase. The thermal conductivity of the sample was subsequently determined through the meticulous analysis of the temperature signal using finite element simulations of the heat conduction equation. Furthermore, the thermal transport properties of the PMMA and SiO_2 layers are also included in the numerical simulations, and these considerations did not adversely affect the thermal conductivity analysis conducted in this study ("Methods" and Supplementary Note 1). Notably, since the electron thermal conductivity in the heterojunction is minimal[31], the measured lattice thermal conductivity is attributed to phonon thermal conductivity.

In order to investigate the thermal conductivity of the whole heterojunction under different bias conditions, an additional voltage (V_3 in Fig. 1a) was introduced across the sample to inject carriers. The thermal conductivity was evaluated under applied bias voltages of 0 V, −9.2 V, and +13.3 V within a high vacuum chamber maintaining a pressure of 10^{-4} Pa, as illustrated from e to g in Fig. 1. The thermal conductivity at 288 K under reverse bias condition was determined for the $MoSe_2$-WSe_2 heterojunction, as well as for the pure $MoSe_2$ and pure WSe_2, to be 15.7 W/mK, 42.2 W/mK, and 45.0 W/mK, respectively. These values were adopted as a benchmark for normalizing the thermal conductivity measurements under varying conditions. The experimental data revealed that for both pure $MoSe_2$ and pure WSe_2, the alteration in thermal conductivity due to the application of reverse and forward bias voltages relative to the zero-bias condition does not exceed 3%. This finding indicates that the thermal conductivity of these two pure materials is essentially unchanged under the influence of an electric field applied in this study and is insensitive to the direction of the electric field.

Upon the formation of a heterojunction between $MoSe_2$ and WSe_2, a notable transformation in their behavior is observed. Prior studies have documented that the $MoSe_2$-WSe_2 heterojunction forms a natural p-n junction with a pronounced electrical rectification behavior[31]. Thermal conductivity measurements indicate that the discrepancy in thermal conductivity between the material under reverse bias (electrical cutoff state) and under zero bias conditions is minimal, remaining within a 3% threshold, as anticipated. Conversely, under forward bias conditions (electrical conduction state), the thermal conductivity of the sample significantly decreases compared to that under zero bias and reverse bias. This reduction becomes more pronounced with decreasing temperature. At 258 K, the thermal conductivity under forward bias is 13.8% lower than that under reverse bias. Such findings suggest that the direction of the applied bias voltage effectively alters the thermal conductivity of the $MoSe_2$-WSe_2 heterojunction. To further substantiate the active and reversible nature of our manipulation method, another Sample #4 is used to investigate the effects of different bias voltages on the thermal conductivity of the heterojunction. The dynamic phonon transport modulation is achieved over a wide range of bias voltages, from −20 V to +15 V (Supplementary Note 2).

Device simulation for $MoSe_2$-WSe_2 heterojunctions

To elucidate the experimental phenomenon of reduced thermal conductivity at electrical forward bias, we propose a first-principles-based computational model. For 2D semiconductor materials under moderate doping conditions, lattice thermal conductivity is primarily influenced by phonon-phonon and phonon-carrier (i.e., electron and hole) scattering[22,36]. The expression for lattice thermal conductivity is given by $\kappa_{lat} = \sum_\lambda c_{V,\lambda} \upsilon_\lambda^2 \tau_\lambda$, where $c_{V,\lambda}$ and υ_λ are the volumetric heat capacity and group velocity of a specific phonon mode λ. τ_λ is the phonon relaxation time, related to the phonon-phonon scattering rate $1/\tau_\lambda^{pp}$, phonon-electron scattering rate $1/\tau_\lambda^{pe}$ and phonon-hole scattering rate $1/\tau_\lambda^{ph}$. Based on Matthiessen's rule, the phonon relaxation time is shown as $1/\tau_\lambda = 1/\tau_\lambda^{pp} + 1/\tau_\lambda^{pe} + 1/\tau_\lambda^{ph}$. The phonon-phonon scattering rate is primarily associated with the lattice vibration, while the phonon-electron (hole) scattering rate also depends on the electron (hole) states. The expression for the phonon-electron (or phonon-hole) scattering rate, based on first-principles Boltzmann transport theory, is as follows[9],

$$\frac{1}{\tau_\lambda^{pe/ph}} = \frac{2\pi}{\hbar} \sum_{\mathbf{k},m,n} \left| g_{m\mathbf{k}+\mathbf{q},n\mathbf{k}}^{\lambda} \right|^2 \left(f_{n\mathbf{k}} - f_{m\mathbf{k}+\mathbf{q}} \right) \times \delta\left(\varepsilon_{n\mathbf{k}} - \varepsilon_{m\mathbf{k}+\mathbf{q}} + \hbar\omega_\lambda \right), \tag{1}$$

where $\left| g_{m\mathbf{k}+\mathbf{q},n\mathbf{k}}^{\lambda} \right|$ is the electron-phonon coupling matrix element, calculated by the density functional perturbation theory (Methods). ε and $\hbar\omega$ are the energy for the electrons and phonons in a scattering event. $f_{n\mathbf{k}}$ and $f_{m\mathbf{k}+\mathbf{q}}$ are the electron distributions related to temperature, carrier concentration, and external field in the heterojunction system.

To determine the carrier concentration and electric field distribution, we first performed the device simulation on the 2D $MoSe_2$-WSe_2 heterojunction system based on the experimental structure (Fig. 1b), as illustrated in Fig. 2a (Detailed settings discussed in Methods). The n-type $MoSe_2$ and p-type WSe_2 form a natural p-n junction with type-II band alignment at the interface (Supplementary Fig. S3), and the simulated current-voltage (I–V) curves at room temperature quantitatively match the experimental measurements (Supplementary Fig. S4). The carrier concentration in the $MoSe_2$-WSe_2 heterojunction at zero bias (Fig. 2c), reverse bias (Fig. 2b), and low forward bias (at $V_a = 0.2$ V, Supplementary Fig. S5) approximately follow the carrier concentration distribution characteristics of an ideal PN junction[37]. However, under larger forward bias conditions (Fig. 2d), the electron and hole concentrations in the $MoSe_2$ and WSe_2 regions increase significantly, exceeding the evenly doping concentration ($2 \times 10^{10}/cm^2$), indicating a high injection regime[38]. The average concentrations of electrons and holes in the $MoSe_2$ region are $5.16 \times 10^{10}/cm^2$ and $4.07 \times 10^{10}/cm^2$, respectively, while in the WSe_2 region, they are $3.16 \times 10^{10}/cm^2$ and $4.06 \times 10^{10}/cm^2$, significantly higher than at zero bias and reverse bias (Supplementary Table. S2).

Furthermore, under large forward bias conditions, there exists an electric field (~10^4 V/cm, supplementary Fig. S6) within the heterojunction, where electrons acquire energy and generate a current in response to the external electric field. Due to the complexity in accurately describing electron behavior in heterojunctions[21], we adopt the equivalent electron temperature model, which is well-accepted in semiconductor device simulations[37,39], illustrated in Fig. 2e. In this model, the electrons (or holes) are assumed to be in equilibrium at an equivalent electron temperature T_e, representing the energy acquired under an electric field. At zero bias or reverse cutoff, where minimal current is generated, electrons (or holes) and phonons are essentially in thermal equilibrium. Hence, the electron and phonon temperatures (T_{lat}) are nearly equal to the ambient temperature ($T_e = T_{lat}$). However, under forward bias conditions, electrons gain energy and occupy higher energy state, while phonons can be considered to remain at the ambient temperature, resulting in $T_e > T_{lat}$.

Thermal conductivity calculations for $MoSe_2$ and WSe_2 regions in the heterojunction

To quantitatively analyze the impact of carrier concentrations and electron temperatures on the thermal conductivity, we first divide the heterojunction into two regions: n-type $MoSe_2$ and p-type WSe_2, and separately consider their thermal conductivities at an ambient temperature of 258 K. Notably, the carrier concentrations and electron temperatures are obtained based on device simulation results of the heterojunction. In the reverse bias condition, the primary charge carriers are electrons in $MoSe_2$, and holes in WSe_2 (Fig. 2b). The phonon-electron scattering rates in $MoSe_2$ and the phonon-hole scattering rates in WSe_2 can be computed using density-functional perturbation theory and maximally localized Wannier functions[40–42]. The

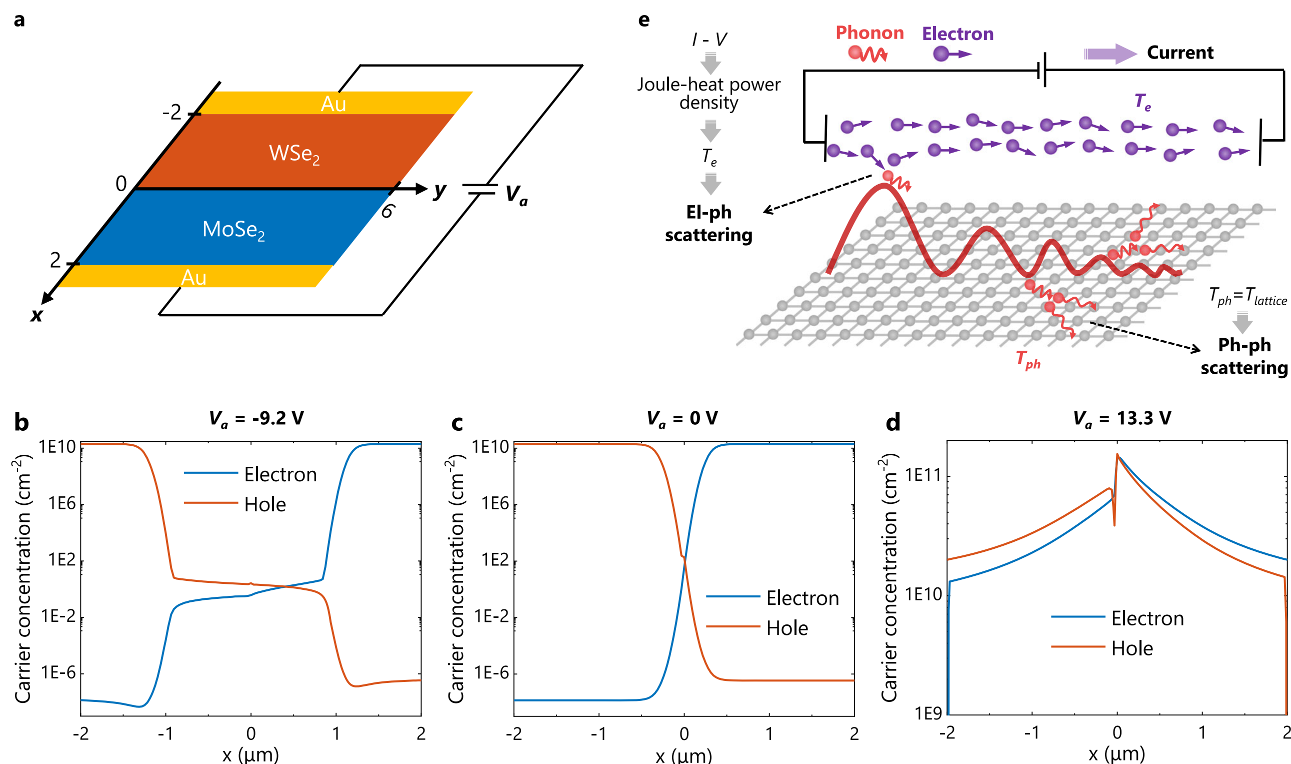

Fig. 2 | Device simulation for $MoSe_2$-WSe_2 lateral heterojunction. a Schematic illustration of the simulated device structure. The $MoSe_2$ and WSe_2 regions are both 2 µm long and 6 µm wide. Gold electrodes are applied to both sides of $MoSe_2$ and WSe_2. A bias voltage V_a is applied. Spatial distribution of electron and hole concentrations along the x direction (cross-section at $y = 0$) under reverse bias (**b**, $V_a = -9.2$ V), zero bias (**c**, $V_a = 0$ V), and forward bias (**d**, $V_a = 13.3$ V) conditions at 258 K. **e** Schematic diagram of the equivalent electron temperature model. Under forward bias conditions, electrons gain energy in the electric field and transfer the energy to phonons. The electron temperature T_e is determined based on the power density of Joule heating and the phonon-electron scattering rate can be calculated. The phonon-phonon scattering rate is calculated at the ambient temperature.

anharmonic lattice dynamics are employed for phonon-phonon scattering rate calculations[43] ("Methods" and Supplementary Note 4). The phonon-phonon and phonon-electron (hole) scattering rates under reverse bias conditions are shown in Fig. 3a, b. The phonon-phonon scattering rates in both materials exhibit an increase with phonon frequency, reaching magnitude on the order of 10^{-1} ps^{-1}. Conversely, the phonon-electron (hole) scattering rates are relatively weak, being lower by more than two orders of magnitude compared to the phonon-phonon scattering rates, thus contributing less to the lattice thermal conductivity. Factoring in both phonon-phonon and phonon-electron (hole) scattering, the lattice thermal conductivity under reverse bias conditions is determined to be 73.2 W/mK for $MoSe_2$ and 66.9 W/mK for WSe_2. The experimentally measured thermal conductivities are lower than the simulation values due to the increased phonon scattering channels provided by the supporting SiO_2 layer[44].

In the forward bias condition, a substantial current density (48.7 µA) is achieved by applying a positive voltage of 13.3 V (Supplementary Fig. S7), and the electron and hole concentrations in both $MoSe_2$ and WSe_2 are significantly higher than those in the reverse bias condition (Fig. 2d). Phonon-phonon, phonon-electron, and phonon-hole scattering need to be simultaneously considered. To calculate the phonon-electron (hole) scattering rates, it is also necessary to determine the equivalent electron temperature (T_e). In this heterojunction, where no luminescent effects or electromagnetic radiation were present, the energy supplied by the voltage is ultimately converted into Joule heat through electron (hole)-phonon interactions (Average power density: 2.70×10^7 W/m^2, Supplementary Note 5). By utilizing first-principles method to compute the electron-phonon energy generation process, the relationship between T_e and the Joule heating power density per unit area of the heterojunction is established (Methods), as shown in Fig. 3c. At an ambient temperature of 258 K and $V_a = 13.3$ V, T_e in $MoSe_2$ is 330 K, while in WSe_2 it is 563 K. The corresponding phonon-electron (hole) scattering rates for both materials are shown in Fig. 3a, b. Under the forward bias condition, there is a significant increase in the phonon-electron scattering rates compared to the reverse cutoff. For some phonon modes (near the Γ point, or around the normalized frequencies 0.4 and 0.8), the phonon-electron (hole) scattering rates are essentially equivalent to the phonon-phonon scattering rates. The total lattice thermal conductivity of $MoSe_2$ is 60.7 W/mK, and that of WSe_2 is 46.9 W/mK. Compared to reverse bias, the thermal conductivity under forward bias decreases by 17.1% in $MoSe_2$ and 29.9% in WSe_2, primarily due to the increased carrier concentrations and elevated electron temperatures (Supplementary Tables S2, S3 and S5).

Next, we consider the temperature dependence of the lattice thermal conductivity of $MoSe_2$ and WSe_2 regions in the heterojunction. With increasing ambient temperature from 258 K to 318 K, the difference between the forward bias and reverse bias thermal conductivities gradually diminishes Fig. 3d, κ_f/κ_r increases and approaches 1.0, consistent with experimental trends. This can be partially attributed to the strong temperature dependence of phonon-phonon scattering[45]. Moreover, the rise in ambient temperature results in a decrease in carrier concentration at high forward bias conditions (Supplementary Tables S2 and S3). Consequently, as the ambient temperature rises, phonon-phonon scattering gradually dominates over phonon-electron (hole) scattering, and the values of thermal conductivity at forward bias and reverse bias tend to consistent. Notably, due to the lower carrier concentration (~10^8/cm^2, Supplementary Fig. S10) and negligible electron temperature rise under forward bias conditions (Supplementary Note 6), the effect of heterojunction-induced reduction in

https://doi.org/10.1038/s41467-025-57224-8

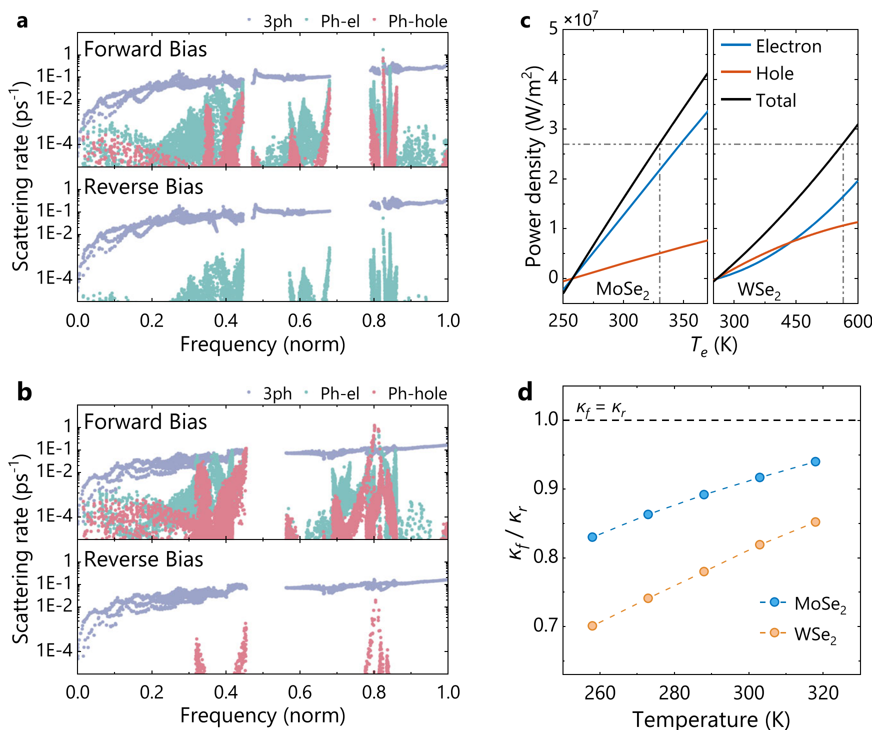

Fig. 3 | First-principles calculation for $MoSe_2$ and WSe_2 regions in the hetero-junction. Phonon-phonon scattering rates (3ph), phonon-electron scattering rates (Ph-el), and phonon-hole scattering rates (Ph-hole) at 258 K under forward bias and reverse bias conditions (**a**, $MoSe_2$, **b**, WSe_2). Each point in the figures represents a phonon mode. The *x*-axis represents the frequency of the phonon mode relative to the maximum frequency. **c** Electron temperature changes with Joule-heating power density under forward bias condition (V_a = 13.3 V) at 258 K for $MoSe_2$ and WSe_2. The gray dashed line represents the experimentally measured average power density, $2.70{\times}10^7$ W/m^2. **d** Thermal conductivities for $MoSe_2$ and WSe_2 regions calculated by first-principles methods change with ambient temperature. κ_f/κ_r represents the ratio of forward bias thermal conductivity to reverse bias thermal conductivity at the same ambient temperature.

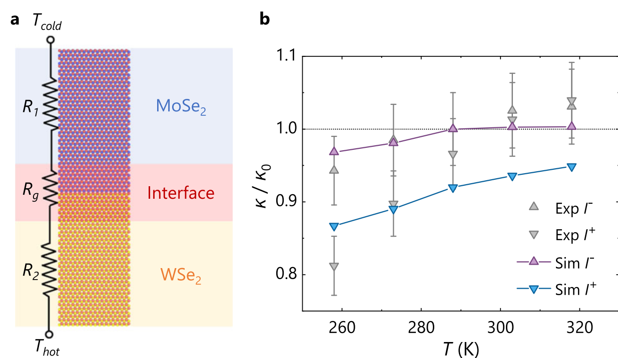

Fig. 4 | Temperature-dependent thermal conductivity calculations for the heterojunction. a Thermal resistance-in-series model for the thermal conductivity of the heterojunction, with thermal resistances corresponding to $MoSe_2$, WSe_2, and the interface denoted as R_1, R_2, and R_g, respectively. **b** Comparison of calculated (Sim) and experimental (Exp) thermal conductivities under forward and reverse bias conditions at different ambient temperatures. The upper triangle and lower triangles represent the reverse bias (I^-) and forward bias (I^+) thermal conductivities, respectively. Error bars show experimental uncertainties of ±5%. The thermal conductivities in the experiment and simulation are normalized to the corresponding reverse bias thermal conductivities at 288 K (κ_0).

thermal conductivity is difficult to directly observe in the pure material samples (Fig. 1f, g).

Temperature-dependent thermal conductivity calculations for $MoSe_2$-WSe_2 heterojunction

Next, we consider the thermal conductivity of the complete hetero-junction. Due to interfacial doping, an interfacial region forms at the junction of $MoSe_2$ and WSe_2, contributing to interfacial thermal resistance (R_g), thereby influencing the overall lattice thermal conductivity of the heterojunction, as depicted in Fig. 4a. The direct measurement of interfacial thermal resistance in 2D lateral hetero-junctions is challenging[46]. Therefore, we estimate that the interfacial thermal resistance is approximately 1×10^{-7} m^{2}K/W at 258 K, based on experimental measurements of the thermal conductivity of pure $MoSe_2$ and WSe_2, as well as the heterojunction (Supplementary Note 7). With increasing temperature, the enhanced anharmonicity at the interface results in higher phonon transmission thereby reducing interfacial thermal resistance[47,48]. Based on the thermal conductivity measurements and molecular dynamics (MD) simulations[49,50] (Supplementary Note 7), it is found that as the ambient temperature increased from 258 K to 318 K, the interfacial thermal resistance decreased by around 20%, consistent with previously reported temperature dependence trends for 2D heterojunctions[47,51].

Subsequently, using the thermal resistance-in-series model (Fig. 4a), we incorporate the calculated thermal conductivities of the $MoSe_2$ and WSe_2 regions, and the estimated temperature-dependent interfacial thermal resistance values to determine the total thermal conductivities of the heterojunction at different ambient temperatures and bias conditions. These results are compared with the experimental measurements, as shown in Fig. 4b. Both computational and experimental results demonstrate that at lower ambient temperatures (258 K), the thermal conductivity at forward bias in the heterojunction is lower than at reverse bias. As temperature increases, this difference between the two thermal conductivities gradually diminishes. Furthermore, the reverse bias thermal conductivity shows a slight increase with temperature. This phenomenon is attributed to the decrease in interfacial thermal resistance as the ambient temperature rises, thereby mitigating the inhibitory effect of temperature-dependent

phonon-phonon scattering on thermal conductivity. These findings underscore the significant impact of interfacial effect on the thermal conductivity of the heterojunction. Due to the complexity of the interfacial structure, we only provide a preliminary quantitative exploration of its impact mechanism on thermal conductivity. Recent studies have proposed interfacial transport models for electron-phonon interactions[48,52,53] and various methods for tuning interfacial thermal transport, including doping and surface modification[54–56]. Further research is required to gain a more comprehensive understanding of interfacial electron and phonon transport and to achieve more pronounced phonon transport manipulation in heterostructures based on advanced interfacial thermal tuning strategies.

In summary, the active modulation of phonon transport based on bias voltage is experimentally achieved and successfully applied in the $MoSe_2$-WSe_2 heterojunction. Under large forward bias, the lattice thermal conductivity of the heterojunction is significantly lower than that under zero and reverse bias. This effect becomes more pronounced as the temperature decreases. At 258 K, the thermal conductivity under forward bias decreases by 13.8% compared to that under reverse cutoff. Subsequently, based on device simulation in combination with first-principles method, calculations are performed for $MoSe_2$ region, WSe_2 region, and the complete heterojunction. We speculate that the bias-dependent thermal conductivity originates from a significant increase in the phonon-electron (or phonon-hole) scattering rate of the heterojunction under forward bias conditions. The increased carrier concentration and elevated equivalent electron temperature under high forward bias injection both contribute to the phonon-electron (or phonon-hole) scattering rate. Furthermore, our calculation illustrates the significant interfacial effects on the heat conduction of the heterojunction. The bias voltage-based manipulation method holds promise for achieving active and reversible modulation of phonon transport without affecting the material structure and has the potential to be extended to a wider range of materials or structural systems.

Methods

Thermal conductivity measurements

Prior to the measurement of the thermal conductivity of 2D materials, a meticulous calibration of the resistance temperature coefficient of two gold sensors was conducted. The ambient temperature of the experimental apparatus was stringently managed by a vacuum thermoelectric heating and cooling stage (INSTEC, TP102SV-PM-F8, ±0.001 K). By adjusting the electrical power supplied to the gold sensors and fitting the resistance-power curve, the resistance of the gold sensors at zero power was determined through extrapolation, which is also the resistance of the gold sensors at ambient temperature. Subsequently, the resistance temperature coefficient was determined by altering the ambient temperature within the controlled environment and by fitting the resistance-temperature curve.

In the experimental configuration, one gold sensor is actuated as a “heater” by applying a substantial current across its terminals, while another gold sensor is utilized as a “detector” by subjecting it to a minimal current. The Joule heat produced by the “heater” is propagated through the sample to the “detector,” resulting in a measurable temperature increase. The magnitude of this temperature increase is meticulously measured by monitoring the resistance changes of the gold sensor acting as the “detector”. By changing the Joule heating power on the “heater” and fitting the temperature curves of the detector and the heater, the temperature response coefficient β can be obtained. The physical significance of β is the value of the temperature increase of the “detector” for every 1 Kelvin increase in the temperature of the “heater”.

$$\beta = \frac{\Delta T_{\mathrm{detector}}}{\Delta T_{\mathrm{heater}}} \tag{2}$$

Eventually, a steady-state thermal conductivity model was developed within the COMSOL Multiphysics (Supplementary Note 1). The geometric dimensions of the model were meticulously extracted from a scanning electron micrograph of the test specimen. The thermal conductivity values for gold and silicon were incorporated into the model, having been previously measured and calibrated utilizing the methodologies described in a prior scholarly investigation. Experimental data for heating power served as the input for the model. In this configuration, the thermal conductivity of the sample itself represented the sole unknown variable. A consistent internal heat source was applied within the gold sensor to emulate the Joule heat generated by electric current passage. The thermal conductivity of the 2D material can be determined through the process of curve fitting the temperature response coefficient, β.

Device simulations

The device simulation is conducted using a modified drift-diffusion model and calibrated with the experimental measurement at room temperature (303 K). The $MoSe_2$ and WSe_2 regions are both 2 μm long and 6 μm wide based on the experimental SEM figure (Fig. 1b), doped as n-type and p-type, respectively, with a doping concentration of 2×10^{10} cm^2. Gold electrodes are applied to both sides of $MoSe_2$ and WSe_2, each with a length of 0.5 μm. Metallic electrode contacts have minimal impact on the heterojunction’s electrical rectification effect[31]. Therefore, in the device simulation, the metal-semiconductor contacts are simplified to ideal Ohmic contacts. The electron affinities, dielectric constants, bandgaps, and carrier density of states for $MoSe_2$ and WSe_2 are obtained from experimental values or calculated values in relevant literature[31,57–60] (Supplementary Table S4). The high-field saturation model is adopted for mobility[61]. Carrier generation and recombination processes are considered using the Shockley-Read-Hall (SRH) model and Auger recombination in the device simulation[37].

First-principles calculations

The ground states of electrons and phonons in $MoSe_2$ and WSe_2 are computed with Quantum ESPRESSO package[40]. We employ scalar relativistic Optimized Norm-Conservinng Vanderbilt (ONCV) pseudopotentials with the Perdew–Burke–Ernzerhof form of the exchange-correlation functional[62]. DFT-D2 of the Grimme method is applied to describe the van der Waals (vdW) interactions[63]. The lattice constants for $MoSe_2$ and WSe_2 are both 3.32 Å, which is consistent with previous studies[57]. Approximately 15 Å of vacuum is set for the out-of-plane direction in our ground-state calculation. The cutoff energy of the plane wave is set to be 100 Ry and the convergence threshold for the electron energy is set to be 10^{-11} Ry for self-consistent calculation with a Monkhorst Pack **k**-point grid of 24 × 24 × 1. The harmonic force constants are obtained using density functional perturbation theory (DFPT) with a 6 × 6 × 1 **q**-point grid and a threshold of 10^{-16} Ry to guarantee the convergence.

The thermal transport properties are calculated with the anharmonic lattice dynamics approach using ShengBTE package[43]. We use 5 × 5 × 1 supercells with a cutoff of the sixth-nearest atom to calculate the third-order force constants using the finite-difference method. The mode-level phonon-phonon scattering rates are calculated under the relaxation time approximation (RTA) with 100 × 100 × 1 **q**-points grids. Although the iterative method has been demonstrated to be a more accurate approach for calculating phonon thermal conductivity, RTA ensures the effective extraction of scattering rates. The phonon-electron and phonon-hole scattering rates are calculated by the Electron-Phonon Wannier (EPW) package, which is based on the maximally localized Wannier functions (MLWFs) and generalized Fourier interpolation[41,42]. The initial coarse electron-phonon coupling matrix element is calculated with a 24 × 24 × 1 **k**-point grids and 6 × 6 × 1 **q**-point grids. Then the initial coarse matrix element is interpolated into dense 100 × 100 × 1 **k**/**q**-points grids to obtain the mode-

level phonon-electron scattering rate. Note that the **q**-point grids for phonon-phonon scattering rate and phonon-electron scattering rate must be consistent for the total lattice thermal conductivity calculation $\kappa_{lat} = \sum_{\lambda} c_{V,\lambda} \upsilon_{\lambda}^{2} \tau_{\lambda}$, where $1/\tau_{\lambda} = 1/\tau_{\lambda}^{pp} + 1/\tau_{\lambda}^{pe} + 1/\tau_{\lambda}^{ph}$. The details of first-principles calculations can be found in Supplementary Note 4.

Determination of equivalent electron temperature

The equivalent electron temperature (T_e) can be determined from the electron-phonon energy generation process. Applying a forward bias voltage to the heterojunction results in a significant conduction current. The average power density (P) of the device is calculated as $P = V_a \times I/A$, where V_a and I are the applied voltage and current, respectively (Supplementary Note 5). And A is the surface area of the heterojunction. Due to the interaction between electrons and phonons, the power density is eventually converted into Joule heat. Based on first-principles Boltzmann transport theory in combination with equivalent electron temperature model, the average power density, i.e., electron-phonon energy generation rate, can be calculated as[39,64]

$$P = \frac{4\pi}{\hbar V} \sum_{\mathbf{k},m,n,\lambda} \hbar\omega_{\lambda} \left| g_{m\mathbf{k}+\mathbf{q},n\mathbf{k}}^{\lambda} \right|^{2} \{ n_{\lambda} \left(f_{m\mathbf{k}+\mathbf{q}}(T_e) - f_{n\mathbf{k}}(T_e) \right) + f_{m\mathbf{k}+\mathbf{q}}(T_e) \left(1 - f_{n\mathbf{k}}(T_e) \right) \} \delta(E_{n\mathbf{k}} - E_{m\mathbf{k}+\mathbf{q}} + \hbar\omega_{\lambda}), \quad (3)$$

where n_{λ} is the phonon distribution, assumed at the ambient temperature. Note that for simplicity, in each material region, it is assumed that the electron and hole temperatures are the same, and only a single electron temperature is used to represent the average Joule heating effect. As shown in Fig. 3c, when the electron temperature is equal to the phonon temperature (ambient temperature), the electron-phonon energy generation rate is zero, indicating no net energy exchange between the electron and phonon systems. With an increase in electron temperature, the electron-phonon energy generation rate gradually increases, maintaining a monotonically increasing trend. As a result, there is a one-to-one correspondence between the electron temperature (T_e) and the electron-phonon energy generation rate (P). Therefore, by calculating the average power density based on current-voltage relationship, the corresponding electron temperature can be determined. This calculation was implemented by modifying the source code of EPW package[39].

Data availability

The authors declare that the data supporting the findings of this study are available in the main article, Supplementary Information, and Source data file. Source data are provided with this paper.

Code availability

The authors declare that the code supporting the findings of this study is available from the corresponding author upon request.

References

1. Kang, J. S. et al. Integration of boron arsenide cooling substrates into gallium nitride devices. *Nat. Electron.* **4**, 416–423 (2021).
2. Kim, S. E. et al. Extremely anisotropic van der Waals thermal conductors. *Nature* **597**, 660–665 (2021).
3. Snyder, G. J. & Toberer, E. S. Complex thermoelectric materials. *Nat. Mater.* **7**, 105–114 (2008).
4. Qian, X., Zhou, J. & Chen, G. Phonon-engineered extreme thermal conductivity materials. *Nat. Mater.* **20**, 1188–1202 (2021).
5. Chen, Z., Zhang, X. & Pei, Y. Manipulation of phonon transport in thermoelectrics. *Adv. Mater.* **30**, 1705617 (2018).
6. Kim, H., Park, G., Park, S. & Kim, W. Strategies for manipulating phonon transport in solids. *ACS Nano* **15**, 2182–2196 (2021).
7. Bao, H., Chen, J., Gu, X. & Cao, B. A review of simulation methods in micro/nanoscale heat conduction. *ES Energy Environ.* **1**, 16–55 (2018).
8. Pop, E. Energy dissipation and transport in nanoscale devices. *Nano Res.* **3**, 147–169 (2010).
9. Tritt, T. M. *Thermal conductivity: theory, properties, and applications*. (Springer Science & Business Media, 2005).
10. Hochbaum, A. I. et al. Enhanced thermoelectric performance of rough silicon nanowires. *Nature* **451**, 163–167 (2008).
11. Li, D. et al. Thermal conductivity of individual silicon nanowires. *Appl. Phys. Lett.* **83**, 2934–2936 (2003).
12. Zhou, Y., Dong, Z.-Y., Hsieh, W.-P., Goncharov, A. F. & Chen, X.-J. Thermal conductivity of materials under pressure. *Nat. Rev. Phys.* **4**, 319–335 (2022).
13. Yang, L. et al. Suppressed thermal transport in silicon nanoribbons by inhomogeneous strain. *Nature* **629**, 1021–1026 (2024).
14. Hu, Y., Xu, J., Ruan, X. & Bao, H. Defect scattering can lead to enhanced phonon transport at nanoscale. *Nat. Commun.* **15**, 3304 (2024).
15. Chen, K. et al. Ultrahigh thermal conductivity in isotope-enriched cubic boron nitride. *Science* **367**, 555–559 (2020).
16. Zou, J. & Balandin, A. Phonon heat conduction in a semiconductor nanowire. *J. Appl. Phys.* **89**, 2932–2938 (2001).
17. Ravichandran, N. K. & Broido, D. Exposing the hidden influence of selection rules on phonon–phonon scattering by pressure and temperature tuning. *Nat. Commun.* **12**, 3473 (2021).
18. Ihlefeld, J. F. et al. Room-temperature voltage tunable phonon thermal conductivity via reconfigurable interfaces in ferroelectric thin films. *Nano Lett.* **15**, 1791–1795 (2015).
19. Quan, Y., Yue, S. & Liao, B. Impact of electron-phonon interaction on thermal transport: a review. *Nanoscale Microscale Thermophys. Eng.* **25**, 73–90 (2021).
20. Sadeghi, M. M. et al. Tunable electron–flexural phonon interaction in graphene heterostructures. *Nature* **617**, 282–286 (2023).
21. Lundstrom, M. Fundamentals of carrier transport, 2nd edn. *Meas. Sci. Technol.* **13**, 230–230 (2002).
22. Liao, B. et al. Significant reduction of lattice thermal conductivity by the electron-phonon interaction in silicon with high carrier concentrations: a first-principles study. *Phys. Rev. Lett.* **114**, 115901 (2015).
23. Zhou, J. et al. Direct observation of large electron–phonon interaction effect on phonon heat transport. *Nat. Commun.* **11**, 6040 (2020).
24. Barik, G. & Pal, S. Monolayer transition-metal dichalcogenide Mo1−x W x S2 alloys as efficient anode materials for lithium-ion batteries. *J. Phys. Chem. C.* **122**, 25837–25848 (2018).
25. Barik, G. & Pal, S. 2D MoS2-MoSe2 and MoS2-NbS2 lateral heterostructures as anode materials for LIBs/SIBs. *Appl. Surf. Sci.* **596**, 153529 (2022).
26. Barik, G. & Pal, S. BlueP encapsulated Janus MoSSe as promising heterostructure anode materials for LIBs. *Phys. Chem. Chem. Phys.* **26**, 18054–18066 (2024).
27. Schaibley, J. R. et al. Valleytronics in 2D materials. *Nat. Rev. Mater.* **1**, 1–15 (2016).
28. Yue, S.-Y., Yang, R. & Liao, B. Controlling thermal conductivity of two-dimensional materials via externally induced phonon-electron interaction. *Phys. Rev. B* **100**, 115408 (2019).
29. Sun, Y., Shuai, Z. & Wang, D. Reducing lattice thermal conductivity of the thermoelectric SnSe monolayer: role of phonon–electron coupling. *J. Phys. Chem. C* **123**, 12001–12006 (2019).
30. Lugovskoi, A., Katsnelson, M. & Rudenko, A. Strong electron-phonon coupling and its influence on the transport and optical properties of hole-doped single-layer InSe. *Phys. Rev. Lett.* **123**, 176401 (2019).
31. Zhang, Y. et al. Simultaneous electrical and thermal rectification in a monolayer lateral heterojunction. *Science* **378**, 169–175 (2022).
32. Lv, Q. & Lv, R. Two-dimensional heterostructures based on graphene and transition metal dichalcogenides: synthesis, transfer and applications. *Carbon* **145**, 240–250 (2019).

33. Wang, H. et al. Experimental study of thermal rectification in suspended monolayer graphene. *Nat. Commun.* **8**, 15843 (2017).
34. Li, S. et al. Halide-assisted atmospheric pressure growth of large WSe2 and WS2 monolayer crystals. *Appl. Mater. Today* **1**, 60–66 (2015).
35. Wang, X. et al. Chemical vapor deposition growth of crystalline monolayer MoSe2. *ACS Nano* **8**, 5125–5131 (2014).
36. Sun, J. et al. Weak effects of electron-phonon interactions on the lattice thermal conductivity of wurtzite GaN with high electron concentrations. *Phys. Rev. B* **109**, 134308 (2024).
37. Hess, K. *Advanced theory of semiconductor devices*. (Wiley-IEEE Press, 2000).
38. Manifacier, J., Ardebili, R. & Popescu, C. High level injection phenomena in P–N junctions. *J. Appl. Phys.* **80**, 2838–2846 (1996).
39. Minamitani, E. Ab initio analysis for the initial process of Joule heating in semiconductors. *Phys. Rev. B* **104**, 085202 (2021).
40. Giannozzi, P. et al. QUANTUM ESPRESSO: a modular and open-source software project for quantum simulations of materials. *J. Phys. Condens. Matter* **21**, 395502 (2009).
41. Mostofi, A. A. et al. wannier90: a tool for obtaining maximally-localised Wannier functions. *Comput. Phys. Commun.* **178**, 685–699 (2008).
42. Poncé, S., Margine, E. R., Verdi, C. & Giustino, F. EPW: electron-phonon coupling, transport and superconducting properties using maximally localized Wannier functions. *Comput. Phys. Commun.* **209**, 116–133 (2016).
43. Li, W., Carrete, J., Katcho, N. A. & Mingo, N. ShengBTE: a solver of the Boltzmann transport equation for phonons. *Comput. Phys. Commun.* **185**, 1747–1758 (2014).
44. Zhang, X. et al. Measurement of lateral and interfacial thermal conductivity of single-and bilayer MoS2 and MoSe2 using refined optothermal Raman technique. *ACS Appl. Mater. interfaces* **7**, 25923–25929 (2015).
45. Zulfiqar, M., Zhao, Y., Li, G., Li, Z. & Ni, J. Intrinsic thermal conductivities of monolayer transition metal dichalcogenides MX2 (M = Mo, W; X = S, Se, Te). *Sci. Rep.* **9**, 4571 (2019).
46. Chen, X.-K., Zeng, Y.-J. & Chen, K.-Q. Thermal transport in two-dimensional heterostructures. *Front. Mater.* **7**, 578791 (2020).
47. Liu, X., Gao, J., Zhang, G. & Zhang, Y.-W. Design of phosphorene/graphene heterojunctions for high and tunable interfacial thermal conductance. *Nanoscale* **10**, 19854–19862 (2018).
48. Chen, J., Xu, X., Zhou, J. & Li, B. Interfacial thermal resistance: past, present, and future. *Rev. Mod. Phys.* **94**, 025002 (2022).
49. Thompson, A. P. et al. LAMMPS-a flexible simulation tool for particle-based materials modeling at the atomic, meso, and continuum scales. *Comput. Phys. Commun.* **271**, 108171 (2022).
50. Hu, Y. et al. Unification of nonequilibrium molecular dynamics and the mode-resolved phonon Boltzmann equation for thermal transport simulations. *Phys. Rev. B* **101**, 155308 (2020).
51. Liu, X., Gao, J., Zhang, G. & Zhang, Y.-W. MoS 2-graphene in-plane contact for high interfacial thermal conduction. *Nano Res.* **10**, 2944–2953 (2017).
52. Hopkins, P. E., Beechem, T. E., Duda, J. C., Smoyer, J. L. & Norris, P. M. Effects of subconduction band excitations on thermal conductance at metal-metal interfaces. *Appl. Phys. Lett.* **96**, 011907 (2010).
53. Yu, S., Zhang, J., Tang, Y. & Ouyang, M. Engineering acoustic phonons and electron-phonon coupling by the nanoscale interface. *Nano Lett.* **15**, 6282–6288 (2015).
54. Yang, H., Gao, S., Pan, Y. & Yang, P. Manipulating heat transfer at graphene/silicon interface with nitrogen doping. *Int. Commun. Heat. Mass Transf.* **155**, 107521 (2024).
55. Yang, H., Shen, Y., Li, L., Pan, Y. & Yang, P. Surface modification to induce efficient heat transfer at graphene/silicon heterointerface. *Appl. Therm. Eng.* **238**, 121913 (2024).
56. Shen, Y., Yang, H., Cao, K. & Yang, P. Interlayer surface modification modulating thermal transport at Si/Gr/HEA heterostructure interfaces. *Int. J. Therm. Sci.* **210**, 109565 (2025).
57. Kumar, S. & Schwingenschlogl, U. Thermoelectric response of bulk and monolayer MoSe2 and WSe2. *Chem. Mater.* **27**, 1278–1284 (2015).
58. Rawat, A. & Rawat, B. Multichannel two-dimensional MoS_2 nanosheet MOSFET for future technology node. *IEEE Trans. Electron Dev.* **71**, 3945–3951 (2024).
59. Kim, H.-g. & Choi, H. J. Thickness dependence of work function, ionization energy, and electron affinity of Mo and W dichalcogenides from DFT and GW calculations. *Phys. Rev. B* **103**, 085404 (2021).
60. Shen, Y., Tian, H. & Ren, T. Simulation of MoS2 stacked nanosheet field effect transistor. *J. Semiconduct.* **43**, 082002 (2022).
61. Sheng, Y. et al. Integrating First-principles-based non-Fourier thermal analysis into nanoscale device simulation. *IEEE Trans. Electron Dev.* **71**, 1769–1775 (2024).
62. Perdew, J. P., Burke, K. & Ernzerhof, M. Generalized gradient approximation made simple. *Phys. Rev. Lett.* **77**, 3865 (1996).
63. Grimme, S. Semiempirical GGA-type density functional constructed with a long-range dispersion correction. *J. Comput. Chem.* **27**, 1787–1799 (2006).
64. Mahan, G. D. *Many-particle physics*. (Springer Science & Business Media, 2013).

Acknowledgements

H.Z., S.X., and H.W. acknowledge the support by the National Natural Science Foundation of China (Grant No. 52276072, H.W.) and the National Key Research and Development Program of China (Grant No. 2023YFB4404100, H.W.). Y.S. and H.B. acknowledge the support by the National Natural Science Foundation of China (Grant No. 52476080, H.B.). Q.L. and R.L. acknowledge the support by the National Key Research and Development Program of China (Grant No. 2021YFA1200800, R.L.). The computations in this paper were run on the π 2.0 cluster supported by the Center for High Performance Computing at Shanghai Jiao Tong University.

Author contributions

H.W., R.L., and H.B. conceived, designed, and supervised the research. Y.S. and H.Z. developed the methodology, performed the numerical simulation, analyzed the data, and prepared the manuscript with discussions with S.X., Q.L., H.X., H.W., R.L., and H.B. H.Z., S.X., and Q.L. performed experimental investigations. All authors reviewed, edited, and approved the manuscript.

Competing interests

The authors declare no competing interests.

Additional information

Supplementary information The online version contains supplementary material available at https://doi.org/10.1038/s41467-025-57224-8.

Correspondence and requests for materials should be addressed to Haidong Wang, Ruitao Lv or Hua Bao.

Peer review information *Nature Communications* thanks Sourav Pal, and the other, anonymous, reviewer(s) for their contribution to the peer review of this work. A peer review file is available.

Reprints and permissions information is available at http://www.nature.com/reprints

Publisher's note Springer Nature remains neutral with regard to jurisdictional claims in published maps and institutional affiliations.

Open Access This article is licensed under a Creative Commons Attribution-NonCommercial-NoDerivatives 4.0 International License, which permits any non-commercial use, sharing, distribution and reproduction in any medium or format, as long as you give appropriate credit to the original author(s) and the source, provide a link to the Creative Commons licence, and indicate if you modified the licensed material. You do not have permission under this licence to share adapted material derived from this article or parts of it. The images or other third party material in this article are included in the article's Creative Commons licence, unless indicated otherwise in a credit line to the material. If material is not included in the article's Creative Commons licence and your intended use is not permitted by statutory regulation or exceeds the permitted use, you will need to obtain permission directly from the copyright holder. To view a copy of this licence, visit http://creativecommons.org/licenses/by-nc-nd/4.0/.

© The Author(s) 2025